

Controlling Deformable Objects with Non-negligible Dynamics: a Shape-Regulation Approach to End-Point Positioning

Sebastien Tiburzio[†], Tomás Coleman[†], Daniel Feliu-Talegon[†], Cosimo Della Santina^{†,‡}

Abstract—Model-based manipulation of deformable objects has traditionally dealt with objects while neglecting their dynamics, thus mostly focusing on very lightweight objects at steady state. At the same time, soft robotic research has made considerable strides toward general modeling and control, despite soft robots and deformable objects being very similar from a mechanical standpoint. In this work, we leverage these recent results to develop a control-oriented, fully dynamic framework of slender deformable objects grasped at one end by a robotic manipulator. We introduce a dynamic model of this system using functional strain parameterizations and describe the manipulation challenge as a regulation control problem. This enables us to define a fully model-based control architecture, for which we can prove analytically closed-loop stability and provide sufficient conditions for steady state convergence to the desired state. The nature of this work is intended to be markedly experimental. We provide an extensive experimental validation of the proposed ideas, tasking a robot arm with controlling the distal end of six different cables, in a given planar position and orientation in space.

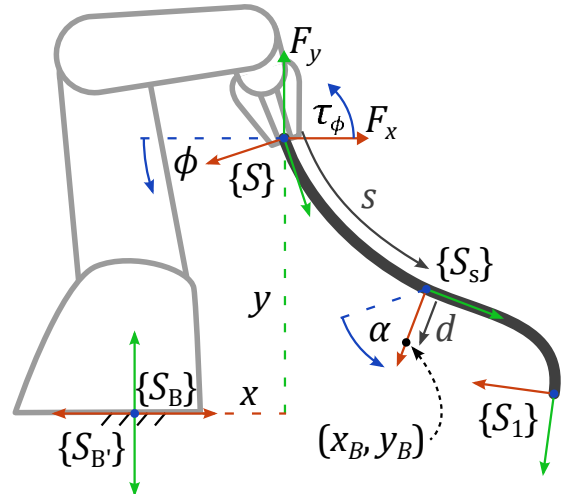


Fig. 1: Pictorial representation of the task that we investigate in this work: the manipulation of slender deformable objects via a generic manipulator holding them at one of their ends by its end effector. We superimpose the important reference frames.

I. INTRODUCTION

Deformable objects are ubiquitous in our daily lives, but robots still find it extremely complex to manipulate them [1]–[4]. A central reason for this difficulty is the need for infinite degrees of freedom (DoFs) to fully describe a deformable object’s state, making the direct application of established strategies unfeasible [5]–[8].

This is the case also for the simplest object geometries that we will be the focus of the present work: slender or deformable

linear¹ objects (DLOs). These are deformable bodies whose spatial configuration can be largely specified in one dominant spatial dimension.

A substantial body of literature focuses on very lightweight, small, or slowly-moving DLOs (i.e., quasi-static regimes). These assumptions allow circumventing the challenge of formulating their dynamics by focusing on purely kinematic descriptions [9]–[13], usually relying on the deformation Jacobian paradigm and shape servoing. Interestingly, [14] extends differential geometry to model linear object deformation—including flexure, torsion, and extension—for grasping and path planning. However, it remains limited to static cases, where inertia can be neglected. Machine learning-based variations of this general approach have also been considered [12], [15]. Learning strategies are nowadays a common choice when it comes to relaxing the quasi-static hypothesis to move into the dynamic manipulation realm [16]–[24]. However, learning-based control comes with its own well-known limitations.

The research was financially supported in part by the Dutch Research Foundation (NWO) through the VENI grant ROSES 20297, as part of Project EMERGE and in part by the European Union (ERC, RIPLEY, 101165078). Views and opinions expressed are however those of the author(s) only and do not necessarily reflect those of the European Union or the European Research Council. Neither the European Union nor the granting authority can be held responsible for them. We are also very grateful for this support. We also thank the company ROCSYS for sharing with us the electric cables used in the experimental validations of our method.

This paper has supplementary downloadable material available at <http://ieeexplore.ieee.org>, provided by the authors. This includes a video showing the performance of the proposed modeling and control strategies. Additional figures and video materials relevant to the results are available at https://github.com/sebtiburzio/PAC_model_matlab/tree/main/appendices

[†]Department of Cognitive Robotics, Delft University of Technology, Delft, The Netherlands. c.dellasantina@tudelft.nl

[‡]Institute of Robotics and Mechatronics, German Aerospace Center (DLR), 82234 Oberpfaffenhofen, Germany.

¹It is worth stressing that *linear* does not refer to the dynamics or kinematics of these systems being linear, but to the fact that these objects *look like* a curved line. In fact, their dynamics are highly nonlinear, as we will discuss later in the paper. To avoid confusion, we sometimes employ the less common denomination of *slender object*.

Some of them are the lack of guarantees, the need for large amounts of data, and the potential safety concerns of the learning process.

This work aims to introduce and experimentally validate a fully control-oriented model-based perspective on manipulating slender deformable objects that does not require applying any quasi-static assumption on the object's behavior. To achieve this goal, we put ourselves in the context of classical control of deformable mechanical systems [14], [25]–[30]. More precisely, we borrow from recent advancements in model-based control of soft robots [31], which are systems entirely made of continuously deformable soft materials [32], [33]. The past few years have seen an exponential increase in control-oriented models of soft robots [34], [35]. These include shape² [39], [40] and - more recently - strain parametrizations [41]–[44]. In turn, the availability of finite-dimensional interpretable models has driven the flourishing of model-based control techniques [45]–[54] that combine improved performance with theoretical guarantees.

To conclude, we propose a dynamic modeling framework for slender objects that have been pre-grasped at one of their ends by a generic robotic manipulator (see Fig. 1). The framework uses strain-based functional parameterization to model DLOs with a non-negligible dynamic response. We then cast the manipulation challenge as a regulation control problem and introduce a control architecture (see Fig. 2), for which we analytically prove closed-loop stability. Compared to recent works [55]–[58] proposing control schemes within a dynamic context for single- and dual-arm DLO manipulation, our work: 1) proves closed-loop stability with explicit conditions, 2) models coupled robot-object dynamics with stability guarantees, and 3) includes gravity effects, analyzing behavior in gravity-influenced planes.

Finally, our principal goal is to showcase the possibilities that pursuing a model-based control route can yield. So, the key feature of this work is to extensively validate the proposed model in static and dynamic regimes and the control strategy when applied to object endpoint position and orientation regulation. Our setup (see Fig. 4) comprises a 7-DoF robot manipulator that grasps high-voltage electric cables normally used for charging electric vehicles.

In a broad sense, this paper can be considered the journal extension of the conference paper [59]. We preliminarily explored these ideas there, even if in a substantially simplified context and with different methods and goals.

II. STRAIN-BASED DYNAMIC MODELING OF DLOs

Our goal is to introduce a fully dynamic model of a robot-object pair as described by Fig. 1. We start by introducing a dynamic model of the object, as it is the part that requires attention, and only at the end do we combine it with the model of the robot.

Compared to the model of a soft manipulator, the object part of the dynamic model introduced in this section presents the extra complexity of not having one of its ends rigidly fixed

to the ground. We can look at this as if the reference frame $\{S\}$ in Fig. 1 is a floating base of the object. We also define a fixed frame representing the manipulator base, $\{S_B\}$, and the three floating base configuration variables $x \in \mathbb{R}$, $y \in \mathbb{R}$ and $\phi \in [-\pi, \pi)$. We consider the nominal state of the object to be hanging vertically downwards from its base, so it is convenient to define an intermediate frame $\{S_{B'}\}$ coincident with $\{S_B\}$ but rotated π radians in the xy plane. When x , y and ϕ are all 0, the object base frame $\{S\}$ is coincident with $\{S_{B'}\}$.

A. Additional assumptions

Here, we consider a few assumptions for the sake of simplicity of derivations but without loss of generality. We considered the object inextensible and not experiencing shear strain in the plane. We also neglect to model any out-of-plane offset curvature and torsional strain, as the gravitational forces dominate in the range of end-effector orientations we validate the model in. We focus on the polynomial curvature functional parameterization [60], which is representative of the general strain case discussed in [42]. Moreover, we propose derivations in the case of planar motions of the object, as this is the case we consider in our experimental validation, and - again - including full motions in 3D only makes derivations more complex without any substantial shift in the core ideas introduced here [61], [62]. Furthermore, the control algorithms that we propose later in this manuscript are agnostic to these simplifying assumptions and can be applied to the general case without modifications.

B. Object's Backbone Kinematics

We describe the DLO shape through its backbone (i.e., its central axis) as the spatial curve $(x_B, y_B, \alpha_B) : [0, 1] \rightarrow \text{SO}(2) \simeq \mathbb{R}^3$, where $s \in [0, 1]$ is the local abscissa along the object. For example, $(x_B, y_B, \alpha_B)(0)$ represents the configuration of the grasped location, $(x_B, y_B, \alpha_B)(1)$ of the one of the other end, and $(x_B, y_B, \alpha_B)(0.5)$ the one of the mid-point.

Using standard results in differential geometry of curves [63], we express the orientation of each point of the backbone as

$$\alpha_B(s) = (\pi + \phi) + \int_0^s \kappa(v) dv, \quad (1)$$

where $\kappa : [0, 1] \rightarrow \mathbb{R}$ is the curvature strain (well-defined thanks to the Lie structure of $\text{SO}(2)$), and $\phi \in S^1 \simeq [-\pi, \pi)$ is the orientation of the grasping location.

Again, relying on the differential geometry of curves [63], the Cartesian coordinates of the central axis are evaluated by integrating components in the x - and y -directions of $\{S_v\}$ as α_B varies up to s

$$\begin{bmatrix} x_B(s) \\ y_B(s) \end{bmatrix} = \begin{bmatrix} x \\ y \end{bmatrix} + L \int_0^s \begin{bmatrix} \sin(\alpha_B(v)) \\ -\cos(\alpha_B(v)) \end{bmatrix} dv \quad (2)$$

where L is the total length of the object, and $x, y \in \mathbb{R}$ are two extra parameters. It is immediate to verify that $(x_B, y_B, \alpha_B)(0) = (x, y, \pi + \phi)$ thus giving an immediate interpretation to the three parameters as the configuration of the robot's end effector.

²Their kinematic version have been independently investigated in deformable objects literature [36]–[38].

Thus, the complete configuration of the object can be reformulated as $(x, y, \phi, \kappa(\cdot))$. Note that, up to this point, the description is exact and infinite dimensional - as κ is a function. We move from infinite to finite domain by approximating the curvature with a Taylor expansion

$$\kappa(s) \simeq \sum_{i=0}^{\infty} \theta_i s^i, \quad (3)$$

which can be truncated to degree n to obtain a finite object configuration vector $\Theta \in \mathbb{R}^{n+1}$ approximating the real object to a desired precision. We use this to express the orientation of the central axis α (relative to the object base frame $\{S\}$) at a normalized distance $s \in [0, 1]$ along the object's length as the integral of the curvature function

$$\alpha(s, \Theta) = \int_0^s \sum_{i=0}^n \theta_i v^i dv \quad (4)$$

The configuration vector for the floating base model combines the curvature and manipulator's end effector variables: $q_O = (\Theta, x, y, \phi) \in \mathbb{R}^{n+4}$.

C. Object's Full Kinematics Under Cosserat Assumption

So far, we have derived the object's kinematic model under the implicit working assumption that it is infinitely thin. This can be readily relaxed under the Cosserat rod description [64] - i.e., we represent the object as nondeforming outside of its central backbone and assume that an undeformable slice of a point mass is rigidly connected at each point of the backbone.

Adding an offset of normalized distance $d \in [-\frac{1}{2}, \frac{1}{2}]$ perpendicular to the central axis, we can then write the forward kinematics for a point on the object, scaling to its physical length L and width D

$$\begin{bmatrix} x_B(s, d) \\ y_B(s, d) \end{bmatrix} = \begin{bmatrix} x \\ y \end{bmatrix} + \begin{bmatrix} L \int_0^s \sin(\alpha_B(s)) dv - Dd \cos(\alpha_B(s)) \\ L \int_0^s -\cos(\alpha_B(s)) dv - Dd \sin(\alpha_B(s)) \end{bmatrix} \quad (5)$$

It is immediate to see that, for $d = 0$, this expression reduces itself to the kinematics of the backbone.

D. Object's Dynamics

Now that the finite-dimensional forward kinematics describing the complete infinite-dimensional shape of the object is defined, we can proceed to establish the dynamics using the Euler-Lagrange methodology. These steps are only briefly summarized here, as they are very similar to the ones detailed in [43], [60]. The inertia matrix is constructed by consideration of the kinetic energy of each infinitesimal mass element in the object:

$$B_O(q_O) = \int_0^1 \int_{-\frac{1}{2}}^{\frac{1}{2}} \rho(s, d) J_{s,d}^T J_{s,d} dd ds. \quad (6)$$

Here $\rho(s, d)$ is the mass density distribution, and $J_{s,d}$ is the Jacobian matrix of the forward kinematics function (5) with respect to q_O . The Coriolis and centrifugal matrix C from the inertia matrix is evaluated by standard procedures - e.g., Christoffel symbols.

The gravitational force field is derived by differentiation of the gravitational potential energy of the infinitesimal masses, with the definition:

$$G_O(q_O) = g \nabla_{q_O} \int_0^1 \int_{-\frac{1}{2}}^{\frac{1}{2}} \rho(s, d) y_B dd ds \quad (7)$$

The direction of the gravitational field is considered directed along $-y$ in the $\{S_B\}$ frame.

We model the object's internal elastic and dissipative forces as discussed in [60]. An addition compared to that model is the relaxation of the assumption that the minimum of the elastic potential is in the straight configuration. Indeed, while this is a reasonable assumption for soft robots, it is not for deformable objects - as we will observe in the experimental validation of our results. This can be simply obtained by introducing an offset $\bar{\Theta}$ in the elastic force term - which is the configuration in which the object would rest when not immersed in a gravitational field.

Combining all these expressions yields the dynamic equations of motion for the floating base system:

$$\begin{aligned} B_O(q_O) \ddot{q}_O + C_O(q_O, \dot{q}_O) \dot{q}_O + G_O(q_O) \\ + \begin{bmatrix} kH & 0_{n+1 \times 3} \\ 0_{3 \times n+1} & 0_{3 \times 3} \end{bmatrix} \begin{bmatrix} \Theta - \bar{\Theta} \\ x \\ y \\ \phi \end{bmatrix} \\ + \begin{bmatrix} \beta H & 0_{n+1 \times 3} \\ 0_{3 \times n+1} & 0_{3 \times 3} \end{bmatrix} \dot{q}_O = \begin{bmatrix} 0_{n \times 1} \\ F_x \\ F_y \\ \tau_\phi \end{bmatrix}, \end{aligned} \quad (8)$$

where F_x , F_y , and τ_ϕ are generalized forces (two forces and torque) representing the action of the robot on the object, H is the $n \times n$ Hankel matrix, and the internal stiffness and damping coefficients of the object averaged along its length are k and $\beta \succ 0$.

E. Complete Dynamical Model

An object dynamics in the form expressed by (8) is extremely convenient when - as for our experimental setup - a force/torque sensor collocated at the gripper location is available that can directly measure F_x, F_y, τ_ϕ .

However, we want to be able to design controllers and assess stability when considering the complete robot-object system dynamics. First, we express the object's forward kinematics as a function of the robot configuration $q_r \in \mathbb{R}^{n_r}$. This is achieved by plugging $(x, y, \phi) = h_r(q_r)$ in (5) with $h_r: \mathbb{R}^{n_r} \rightarrow \text{SO}(3)$ being the forward kinematics of the robot's end effector.

Then, the full-order dynamics is readily derived by differentiating separately w.r.t. q_r and Θ the new kinetic and potential energies so defined

$$\begin{aligned} \begin{bmatrix} B_{r,r}(q_r, \Theta) & B_{r,\Theta}(q_r, \Theta) \\ B_{r,\Theta}^T(q_r, \Theta) & B_{\Theta,\Theta}(\Theta) \end{bmatrix} \begin{bmatrix} \ddot{q}_r \\ \ddot{\Theta} \end{bmatrix} + C(q_r, \Theta, \dot{q}_r, \dot{\Theta}) \begin{bmatrix} \dot{q}_r \\ \dot{\Theta} \end{bmatrix} \\ + \begin{bmatrix} 0_{n_r \times 3} & 0_{n+1 \times n_r} \\ 0_{n_r \times n+1} & \beta H \end{bmatrix} \begin{bmatrix} \dot{q}_r \\ \dot{\Theta} \end{bmatrix} + \begin{bmatrix} G_r(q_r, \Theta) \\ G_\Theta(q_r, \Theta) \end{bmatrix} \\ + \begin{bmatrix} 0_{n_r \times 3} & 0_{n+1 \times n_r} \\ 0_{n_r \times n+1} & kH \end{bmatrix} \begin{bmatrix} q_r \\ (\Theta - \bar{\Theta}) \end{bmatrix} = \begin{bmatrix} \tau \\ 0_{n+1 \times 1} \end{bmatrix}. \end{aligned} \quad (9)$$

where $(q_r, \Theta) \in \mathbb{R}^{n_r+n+1}$ is the full order counterpart of q_O and complete configuration of the robot-object system.

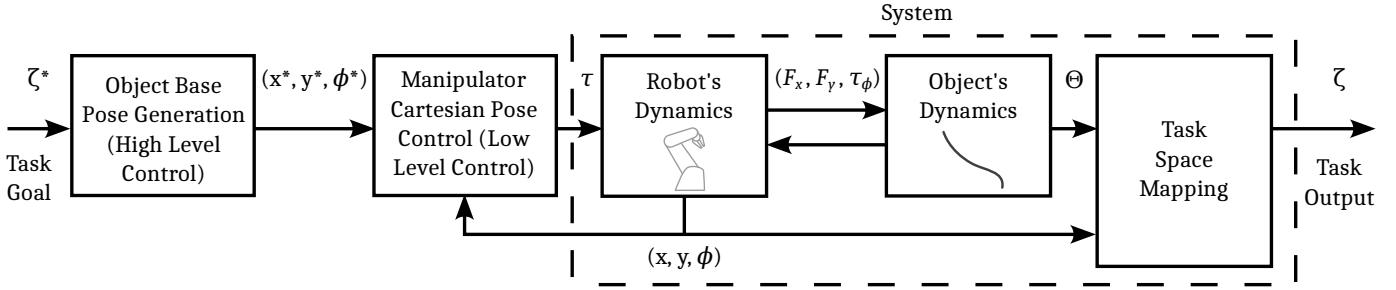


Fig. 2: A block diagram outline of the control strategy. The input is a task goal ζ^* which can be achieved by regulation of the object's shape. We use a nonlinear model-constrained optimization to map this to a Cartesian object base pose (x^*, y^*, ϕ^*) , providing a control input to the coupled manipulator-object system.

The other elements of the equation have their meaning in accordance with previous definitions.

Two facts about (9) are worth stressing here. First, the object and the robot are coupled purely through the potential field and the inertia forces. No elastic or dissipative coupling between the two dynamics is present.

Second, writing the operational space dynamics of the robot from (9) and equating it to (8) allows us to prove that

$$(q_r, \dot{q}_r) \equiv 0 \Rightarrow (F_x, F_y, \tau_\phi) = [0_{3 \times n+1} \quad I_{3 \times 3}] G_O. \quad (10)$$

III. MANIPULATION AS CLOSED-LOOP CONTROL

The general control architecture proposed in this work is presented in Fig. 2. In the following, we present its main components step by step. In the process, we discuss the stability and convergence properties of a broad class of controllers that can be applied to this setting.

A. Task Goal

Thanks to the effort to establish a complete model of the robot-object pair in Sec. II, we can now define our manipulation goal as a shape regulation task. More precisely, we wish to define a policy that specifies the control action τ in (9) such that

$$\lim_{t \rightarrow \infty} \zeta(x, y, \phi, \Theta) = \zeta^*. \quad (11)$$

Here, $\zeta : \mathbb{R}^{n+4} \rightarrow \mathbb{R}^m$ is a generic representation of a object-centric task. In other words, the configuration of the robot affects the fulfillment of the task only to the extent to which a change of q_r reflects a change in the robot's state. This can, for example, be the position and orientation of one or more points along the object structure (we consider this case in the experimental validation), their relative position to an external target (e.g., insertion task), or directly the object shape Θ .

B. Low-level Control

At this stage, we use the control inputs τ to regulate the collocated configuration variables q_r . Our goal for this section is to analyze the closed-loop control problem and propose a simple but provably stable control strategy. This layer will then be used by the high-level controller to ultimately solve the control goal stated above.

1) *Stability of the zero dynamics*: Combining (8) and (10) yields the zero dynamics

$$B_{\Theta, \Theta}(\Theta) \ddot{\Theta} + C_{\Theta, \Theta}(\Theta, \dot{\Theta}) \dot{\Theta} + \beta H \dot{\Theta} + G_{\Theta}(\Theta, \phi^*) + kH(\Theta - \bar{\Theta}) = 0. \quad (12)$$

Where ϕ^* is the end effector orientation associated with the fixed robot configuration q_r^* . This equation describes the behavior of the object when the robot is fixed in some configuration, and analyzing its stability is a fundamental step in designing a robot-side controller and assessing its performance. We do this in the following proposition.

Proposition 1: The state $(\Theta^*, 0) \in \mathbb{R}^{2n}$ is an asymptotically stable equilibrium of (12) if an open neighborhood $\mathcal{N}(\Theta) \subseteq \mathbb{R}^2$ of Θ^* exists such that $\forall \Theta \in \mathcal{N}(\Theta^*) / \{\Theta^*\}$

$$(U_{G_{\Theta}}(\Theta, \phi^*) + U_K(\Theta)) > (U_{G_{\Theta}}(\Theta^*, \phi^*) + U_K(\Theta^*)) + \left(\frac{\partial}{\partial \Theta} (U_{G_{\Theta}}(\Theta, \phi^*) + U_K(\Theta)) \right) \Big|_{\Theta=\Theta^*}^T (\Theta - \Theta^*) \quad (13)$$

where $U_{G_{\Theta}}$ and U_K represent the potential energy associated with gravity and elasticity of the DLO, respectively.

Proof 1: Taking inspiration from the soft robotics literature, we propose to use a modified version of the Lyapunov function in [31, Theorem 1], which is

$$V = \frac{1}{2} \dot{\Theta}^T B_{\Theta, \Theta} \dot{\Theta} + U_{G_{\Theta}}(\Theta, \phi^*) - U_{G_{\Theta}}(\Theta^*, \phi^*) + U_K(\Theta) - U_K(\Theta^*) + (kH(\Theta^* - \bar{\Theta}) + G_{\Theta}(\Theta^*, \phi^*)) (\Theta^* - \Theta). \quad (14)$$

Taking into account condition (13) and the fact that the kinetic energy is always strictly positive definite in $\dot{\Theta}$, it follows that V is positive definite. Next, we analyze the sign of its time derivative, which is

$$\begin{aligned} \dot{V} &= \frac{1}{2} \dot{\Theta}^T \dot{B}_{\Theta, \Theta} \dot{\Theta} + \dot{\Theta}^T B_{\Theta, \Theta} \ddot{\Theta} + \dot{\Theta}^T (kH(\Theta - \bar{\Theta}) + G_{\Theta}(\Theta, \phi^*)) \\ &\quad - \dot{\Theta}^T (kH(\Theta^* - \bar{\Theta}) + G_{\Theta}(\Theta^*, \phi^*)) \\ &= \frac{1}{2} \dot{\Theta}^T \dot{B}_{\Theta, \Theta} \dot{\Theta} + \dot{\Theta}^T (kH(\Theta - \bar{\Theta}) + G_{\Theta}(\Theta, \phi^*)) \\ &\quad + \dot{\Theta}^T (-C_{\Theta, \Theta} \dot{\Theta} - kH(\Theta - \bar{\Theta}) - G_{\Theta}(\Theta, \phi^*) - \beta H \dot{\Theta}) \\ &= -\dot{\Theta}^T \beta H \dot{\Theta} \leq 0, \end{aligned} \quad (15)$$

where we leverage the system's passivity, as expressed by $\dot{B}_{\Theta,\Theta} - 2C_{\Theta,\Theta} = 0$, and the equilibrium condition $kH(\Theta^* - \bar{\Theta}) + G_{\Theta}(\Theta^*, \phi^*) = 0$. Consequently, equation (15) is shown to be negative semidefinite, but thanks to LaSalle's principle, we can guarantee that the system converges to the set $(\Theta^*, 0)$, provided that the equilibrium configuration Θ^* is the only configuration in $\mathcal{N}(\Theta^*)$ satisfying $\dot{\Theta} = 0$ for $\dot{\Theta} = 0$. \square

Then, the collocated zero dynamics (12) is such that

$$\lim_{t \rightarrow \infty} \dot{\Theta} = 0 \quad (16)$$

if $\beta > 0$.

2) *Control strategy*: The stability of the zero dynamics enables direct feedback linearization to regulate the robot's states. However, we prefer here a simpler regulator that extends controllers commonly used in industrial robots.

$$\tau = K_P(q_r^* - q_r) + K_D(-\dot{q}_r) + G_r(q_r, \Theta). \quad (17)$$

where $K_P, K_D \succ 0$ are two positive definite control gain matrices. The only condition necessary for the closed loop stability is that $\beta > 0$.

Proposition 2: There always exist a large-enough proportional gain K_P such that the trajectories of the closed-loop system (17), (9) are bounded and converge asymptotically to the equilibrium state $(q_r^*, \Theta^*, 0, 0)$, where Θ^* is a solution of

$$G_{\Theta}(\Theta^*, \phi^*) + kH(\Theta^* - \bar{\Theta}) = 0. \quad (18)$$

Proof 2: The proof follows directly from Proposition 1, following the same steps of the proof of Theorem 1 in the soft robotics control paper [65]. \square

Furthermore, we can provide even stronger convergence properties for the closed loop under slightly stronger hypotheses, as discussed in the following proposition.

Proposition 3: The closed loop (17), (9) converges asymptotically to the unique solution of (18) in the region of attraction \mathcal{N} , if

$$\left(kH + \frac{\partial G_{\Theta}(\Theta, \phi^*)}{\partial \Theta} \right) \succ 0, \quad \forall \Theta \in \mathcal{N}. \quad (19)$$

Proof 3:

The statement has two parts. The first one is that the solution in \mathcal{N} is unique. This follows by the application of Hadamard's global inverse function theorem since the left-hand side of (19) is the Jacobian of the left-hand side of (18). Also, the left-hand side of (19) is proper because it is radially unbounded as $\|\Theta\| \rightarrow \infty$, the linear term $kH(\Theta - \bar{\Theta})$ dominates because it grows without bound. This allows to state the property globally if \mathcal{N} coincides with the whole configuration space.

The second part is about asymptotic convergence. This one can be proven by relying on a variation of the Lyapunov candidate that we proposed in the proof of Proposition 1

$$\begin{aligned} V = & \frac{1}{2} \begin{bmatrix} \dot{q}_r \\ \dot{\Theta} \end{bmatrix}^T \begin{bmatrix} B_{r,r}(q_r, \Theta) & B_{r,\Theta}(q_r, \Theta) \\ B_{r,\Theta}^T(q_r, \Theta) & B_{\Theta,\Theta}(\Theta) \end{bmatrix} \begin{bmatrix} \dot{q}_r \\ \dot{\Theta} \end{bmatrix} \\ & + U_{G_{\Theta}}(\Theta, \phi) - U_{G_{\Theta}}(\Theta^*, \phi^*) + U_K(\Theta) - U_K(\Theta^*) \\ & + (kH(\Theta^* - \bar{\Theta}) + G_{\Theta}(\Theta^*, \phi^*)) (\Theta^* - \Theta) \\ & + \frac{1}{2} (q_r^* - q_r)^T K_P (q_r^* - q_r). \end{aligned} \quad (20)$$

The proof then follows similar steps, with the only addition of noticing that (19) implies (13). \square

In the soft robotics literature, (19) is called elastic dominance, and its goal is to ensure that the physical compliance of the robot (or, in this case, of the object) is high-enough when compared to gravity.

Remark 1: The control strategy (17) simplifies to the standard PD control with gravity compensation under the hypothesis that the mass of the object is significantly smaller than the robot's mass. This becomes evident when considering that the gravity terms associated with the robot are the sum of the contributions from the robot's own mass and the effect of the DLO on the robot, expressed as $G_r(q_r, \Theta) = G_{rr}(q_r) + G_{or}(q_r, \Theta)$. If we assume that the mass of the object is significantly smaller than the robot's mass, i.e., $\|B_{\Theta,\Theta}\| \ll \|B_{r,r}\|$, it follows that $G_r(q_r, \Theta) \simeq G_{rr}(q_r)$. This can be further formulated as: $\partial G_r / \partial \Theta \simeq 0$, which is commonly observed in practice, as it reflects the typical scenario where the object's mass is negligible compared to the robot's mass.

C. High-level Control

Employing the low-level controller (17) allows to freely specify a configuration q_r^* for the robot. Combining this capability with standard Jacobian-based Cartesian controllers, we can use this capability to freely specify a configuration of the robot's gripper (x^*, y^*, ϕ^*) .

To avoid destabilizing the low-level control loop, we cast the high-level component as pure feedforward, as outlined in the block diagram of Fig. 2. We propose a model-constrained nonlinear optimization as an object pose generation algorithm. We use the manipulator's grasping point to control the equilibrium shape Θ^* of the object via the steady state zero dynamics equation (18). Note that we can do so because of the pure dependency of G_{Θ} on (x^*, y^*, ϕ^*) rather than on the complete configuration q_r^* .

Our desired object configuration is one such that the control goal (11) is verified. To find such a configuration, we define a cost based on a distance measure between desired and modeled positions and orientations, $d(\zeta^*, \zeta)$.

Thus, the optimization problem can then be written as:

$$\begin{aligned} & \min_{\Theta^* \in \mathbb{R}^{n+1}, (x^*, y^*, \phi^*) \in \mathbb{F}} d(\zeta^*, \zeta(x^*, y^*, \phi^*, \Theta^*)) \\ & \text{s.t. } G_{\Theta}(\Theta^*, \phi^*) + kH(\Theta^* - \bar{\Theta}) = 0. \end{aligned} \quad (21)$$

Here, we also impose a feasible set \mathbb{F} on the floating base coordinates to represent the constrained reachable workspace of the manipulator - thus avoiding the risk of generating unfeasible references to the Cartesian control. This set can also be used to represent environmental constraints.

By solving (21), we retrieve a base configuration (x^*, y^*, ϕ^*) minimizing the difference between the desired and modeled object shape, thus completing the control architecture in Fig. 2.

IV. EXPERIMENTAL VALIDATION OF THE MODEL

A. Experimental Setup

1) *Test Objects*: The DLOs used in our experimental investigations are heavy gauge electrical cables, chosen particularly due to their significant inertia and moderate stiffness.

TABLE I: Object Parameter Variations

ID	m_L [kg]	m_1 [kg]	L [m]	D [m]
OB1	0.6	0.23	0.6	0.02
OB2	0.6	0.03	0.6	0.02
OB3	0.42	0.23	0.4	0.02
OB4	0.42	0.03	0.4	0.02
OB5	0.4	0.23	0.75	0.015
OB6	0.25	0.03	0.45	0.015



Fig. 3: The test objects used in the experiments, OB1-OB6 from left to right. These are high-voltage electric cables used in the context of the electric car industry. The cables end with a plug connector.

Different lengths, gauges (diameter and material composition) and the weight of the endpoint mass provide variation in the object properties leading to a range of different dynamic and equilibrium behaviours. Objects OB1-OB4 are made from the same, thicker cable material, and have variations of both a short or long length, and a significant or minimal endpoint mass. Objects OB5 and OB6 are made from a more flexible material, and only a long, weighted variation and a short, unweighted variation are considered. The full set of objects is pictured in Fig. 3.

The objects considered here are assumed to have constant density and cross-section along their length; however, instead of using the exact continuous distribution of $\rho(s, d)$ when evaluating (6) and (7), we simplify using an approximation of six discrete lump masses. These are equally spaced along the length of the object at positions $s = \{\frac{1}{12}, \frac{3}{12}, \frac{5}{12}, \frac{7}{12}, \frac{9}{12}, \frac{11}{12}\}$, each with a mass of $\frac{m_L}{6}$ distributed across the total diameter. Different masses m_0 and m_1 are also included at $s = 0$ and $s = 1$, to account for separate masses concentrated at the base and end of the object. In terms of unmodeled non-idealities, approximately 0.05-0.1m at the end of the objects is rigid to facilitate the attachment of the endpoint mass. Table I summarises the properties of the objects.

2) *Test Equipment*: A Franka Emika FR3 7-DoF manipulator arm was used to provide actuation of the object's base in

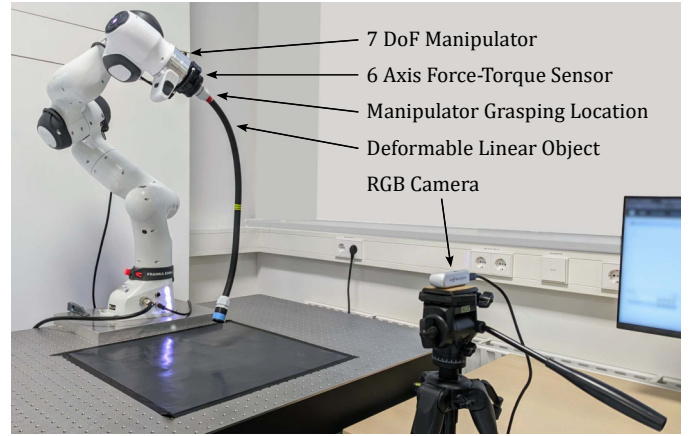


Fig. 4: The experimental setup used for validation of the proposed model and control architecture. Relevant components are highlighted. Note that for simplicity and reproducibility, we are connecting the object directly to the robot's end effector instead of grasping it via a gripper.

the experiments. When required, a Bota Systems SenseOne 6-axis force-torque sensor was assembled in between to measure the actuation applied. An Intel Realsense D435 camera was used to capture RGB images at 30Hz, from which the object state could be extracted. All hardware control and communication were managed through a PC running Ubuntu 20.04 and the ROS Noetic middleware. Fig. 4 shows an overview of the test equipment setup.

B. Extraction of the Object State

Points on the object at $s = \{0, 0.5, 1\}$ and $d = 0$ were identified with coloured markers, facilitating the detection of their pixel locations via HSV thresholding. Under the assumption that the object stays confined to the plane on which the manipulator endpoint moves, the 3D marker positions were determined by intersecting this plane with the line projected through the associated pixel coordinate. The positions of the base, mid-point, and endpoint of the DLO are extracted for two purposes: to estimate the object's curvature and to present results and validate our approach at different points along the DLO.

By taking the recovered 3D marker positions and discarding the third coordinate (in the direction normal to the assumed object plane) we are left with the planar model 2D Cartesian coordinates of the start-, mid- and endpoints of the central axis in $\{S_B\}$: $p_{s,B}$, $p_{m,B}$ and $p_{e,B}$. Note that hereafter we will omit the subscript B , so that any Cartesian coordinates mentioned can be assumed measured in $\{S_B\}$ unless indicated otherwise.

The floating base system configuration best matching the observed points on the object can be extracted via the algorithm 1. The algorithm has the form of a CLIK (closed-loop inverse kinematics) strategy with an over-constrained task space, as the number of target outputs (measurements of the current shape) is higher than the configurations. There, $q_{0,init}$ is an initial guess, p are the measured coordinates of

the three marked points, and $h(q_O)$ and $J(q_O)^+$ evaluate the forward kinematics and Jacobian pseudoinverse respectively at the same locations. Note that the pseudoinverse is here to be intended as a minimum MSE solution. Finally, ϵ and Δ are tuned to a desired accuracy and convergence rate. The calculation time of the Inverse Kinematics algorithm, which was outlined in Algorithm 1 was tested using the parameters identified for OB1. The tests were conducted using polynomial models of order 0 to 4, with an initial guess of $\theta = 0$. The input values of p_m and p_e were taken from the DLO and generated over the range $-\pi \geq \theta_i \geq \pi$. The results of the benchmarked computation times for this algorithm are shown in Fig. 5. The tests were run on an Intel 12th Gen i7-12700H (20) @ 4.600GHz CPU. These results demonstrate that the calculation can feasibly be integrated into a real-time control system, with both accuracy and computation time adjustable by selecting the appropriate polynomial order to suit specific application requirements.

Algorithm 1 Iterative Estimation of the Shape (CLIK-like)

```

 $q_O \leftarrow q_{O,init}$ 
while  $i \leq i_{max}$  do
   $e = \|p - h(q_O)\|_2$ 
  if  $e < \epsilon$  then
    return  $q_O$ 
  else
     $q_O \leftarrow q_O - \Delta J(q_O)^+ e$ 
  end if
end while

```

C. Parameter Identification

The model contains several object-specific parameters, some of which are not easy to directly measure. Measurable parameters are the object length L , diameter D , total mass of the object body m_L , object base mass m_0 , and endpoint mass m_1 . Immeasurable parameters are the object stiffness k , object damping β , and curvature offset $\bar{\Theta}$. To determine the unknown

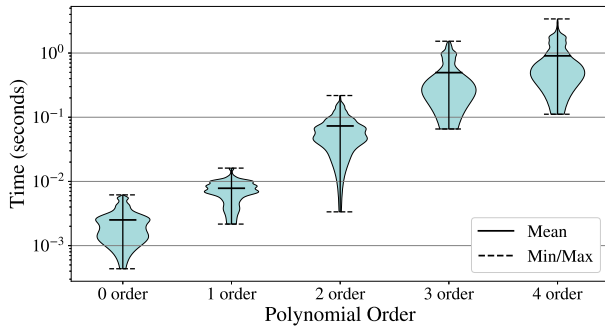


Fig. 5: Distributions of computation times for the inverse kinematics algorithm 1, for various order of approximation. The assumed DoFs for the object are equal to the polynomial order plus one. The time taken to converge to a solution was calculated for 1000 values randomly selected throughout the θ -space.

parameters, an identification procedure was developed in two parts, separating out those that could be determined from the static case and those that require dynamic analysis.

For the static case, the equilibrium state of the object is extracted at a series of discrete base orientation angles ϕ . This data is used to construct a set of linear equations, from which a pseudoinverse solution can be used to determine the values for k and $\bar{\Theta}$, providing a least squares best fit. Equation (22) shows the development of the zero dynamics in (18) into the form used to obtain the pseudoinverse solution. This represents a system of $n + 1$ equations corresponding to a single ϕ , in practice this is extended with additional rows for each ϕ and object state Θ^* measured, before the pseudoinversion step.

$$\begin{aligned}
 G_{\Theta}(\Theta^*, \phi^*) + kH(\Theta^* - \bar{\Theta}) &= 0 \\
 [H\Theta^* \quad -H] \begin{bmatrix} k \\ k\bar{\Theta} \end{bmatrix} &= -G_{\Theta}(\Theta^*, \phi^*) \\
 \begin{bmatrix} k \\ k\bar{\Theta} \end{bmatrix} &= [H\Theta^* \quad -H]^+ (-G_{\Theta}(\Theta^*, \phi^*))
 \end{aligned} \tag{22}$$

With the values of k and $\bar{\Theta}$ estimated as outlined above, identification of the final unknown parameter β can subsequently be done using data taken from a dynamic evolution of the object. The approach is similar, using the zero dynamics (12) to construct an overdetermined system of equations and calculate a pseudoinverse solution as shown in (23).

$$\begin{aligned}
 \beta &= (H\dot{\Theta})^+ (-B_{\Theta,\Theta}(\Theta)\ddot{\Theta} - C_{\Theta,\Theta}(\Theta, \dot{\Theta})\dot{\Theta} - G_{\Theta}(\Theta, \phi^*) \\
 &\quad - kH(\Theta - \bar{\Theta})).
 \end{aligned} \tag{23}$$

D. Comparative analysis of polynomial curvature across different orders

In the proposed approach, the configuration of the slender object is parametrized using polynomial curvature functions (3). While this representation is exact in the infinite-dimensional case, it can be truncated to a polynomial of degree n to yield a finite-dimensional object configuration suitable for real-world applications. In this section, we compare the use of constant, linear, and quadratic curvature models for describing the shape of a real object. For this comparative analysis, we use the object OB1 and identify the equivalent object parameters for the three cases. With a first-order curvature model, the object configuration can be uniquely identified from two points (Section IV-C). For higher-order polynomials, multiple solutions exist, but only one satisfies the equilibrium. We recover parameters by minimizing the error between measured and predicted marker positions over 23 configurations spanning base orientations in $[-\pi, \pi]$, following strategies similar to [66].

The resulting parameters for the three cases are as follows: 1) $k = 0.1726$ and $\bar{\Theta} = -0.0005$, 2) $k = 0.197$ and $\bar{\Theta} = (0.142, 1.24)$ and 3) $k = 0.1695$ and $\bar{\Theta} = (0.1081, 1.5017, 0.0022)$. Fig. 6 presents the results obtained after parameter identification for the three cases. The lower part of Fig. 6 shows the errors at the middle point (Δp_m) and

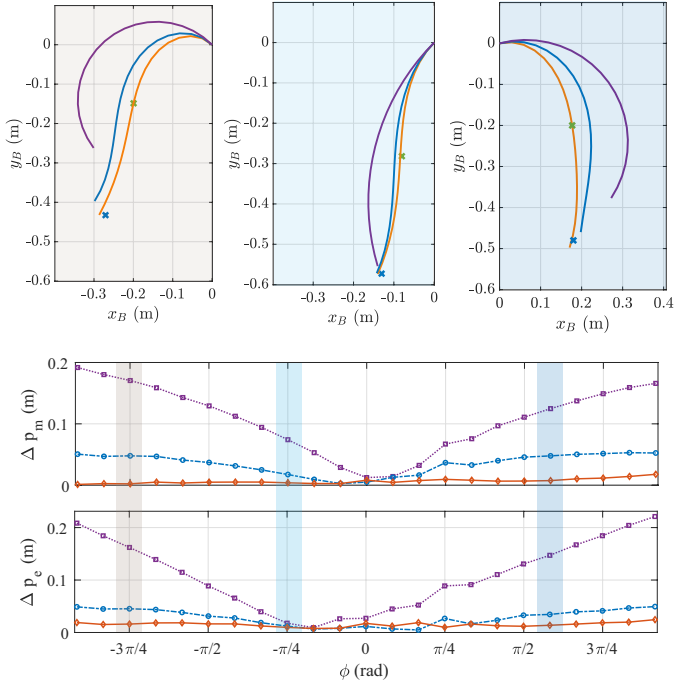


Fig. 6: Comparative analysis of polynomial curvature across different orders. The results are obtained using constant (purple line), linear (blue line), and quadratic curvature (orange line). In the upper part, we show the shapes for three different orientations with colored backgrounds, which correspond to the colored regions in the figure below.

the end-effector of the object (Δp_e), while the upper part illustrates the object's shape for some configurations. The average errors with the standard deviations at the middle point for the three cases are 11 ± 5.5 cm, 3.5 ± 1.6 cm and 1.2 ± 0.4 cm, while at the endpoint they are 11 ± 6.7 cm, 2.9 ± 1.5 cm and 1.5 ± 0.5 cm, respectively. These results effectively demonstrate that increasing the order of the polynomial significantly improves accuracy, particularly in capturing the object's middle point. However, this improvement comes at the cost of increasing the polynomial order, which, in turn, increases the dimensions of the matrices describing the system.

E. Model Validation Results

A polynomial of degree $n = 1$ was used for the experimental validation: an affine curvature strain parametrization [67] of the object shape, where $\Theta = (\theta_0, \theta_1)$. The parameter identification procedures laid out in Section IV-C were carried out using this model. The ultimately determined values are summarised in Table II, while the rest of this subsection will detail the practical considerations and intermediate results.

1) *Steady State*: Static equilibrium datasets were collected for each of the objects at 23 orientations of ϕ , angled at evenly spaced $\frac{\pi}{12}$ rad increments excluding $-\pi$. To minimize the influence of hysteresis on the object's shape between measurements, they were returned to $\phi = 0$ and shaken loose before moving to each measurement orientation. Configurations of Θ corresponding to the measured p_s , p_m and p_e were

then extracted to use as input to the parameter identification formulation for k and $\bar{\Theta}$ as described in Section IV-C. Note that the affine curvature model exhibits parameter-dependent multi-stability [68]. Here, it is generally safe to assume that the object will settle to an expected equilibrium if it begins in a nominal static state at $\phi = 0$ and Θ close to $(0, 0)$, and is rotated slowly within $-\pi \leq \phi < \pi$.

TABLE II: Identified Object Parameters

ID	k	θ_0	θ_1	β
OB1	0.197	0.142	1.24	0.0347
OB2	0.226	-0.0358	2.06	0.0311
OB3	0.253	0.830	-0.452	0.0359
OB4	0.360	0.748	0.0711	0.0454
OB5	0.0761	0.354	0.636	0.0343
OB6	0.269	0.479	0.621	0.0397

Following identification for the static case, we check how well the resulting model predicts the equilibrium behaviour of the real objects. Fig. 7a shows the results of this process for OB1, plotted for $\phi = \{0, \pm \frac{\pi}{4}, \pm \frac{\pi}{2}, \pm \frac{3\pi}{4}\}$ (7 of the 23 datapoints used). Here, the coloured crosses indicate the measured positions of p_m and p_e , and the light orange curves represent the configurations of Θ from inverse kinematics, used in (22) to identify the parameters. The dark orange curves are the steady state of the model obtained by forward simulation using the identified parameters. A composite image of the actual object shapes at these angles is shown in Fig. 7b. Equivalent figures for the other objects are not included for the sake of space, but are available in the extra appendix materials.

The error between the measured and modeled object end effector position, Δp_e , and relative error $\Delta p_e/L$, are plotted against the angle ϕ in Fig. 8 for the each object, providing a measure of the modeling accuracy. The results show that the static equilibrium model provides quite an accurate estimate

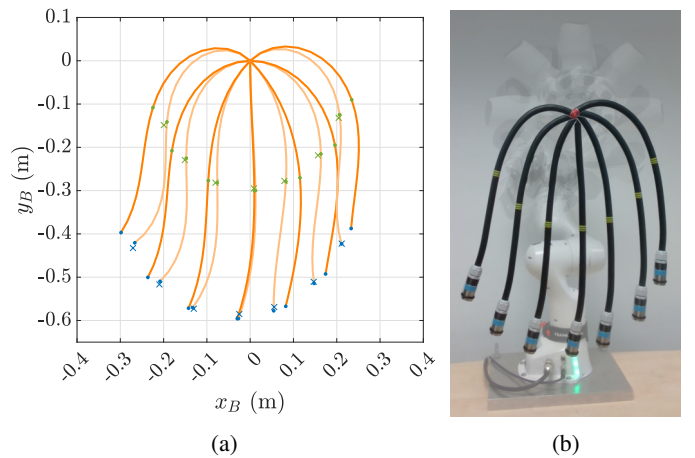


Fig. 7: Comparison of the measured and modeled object equilibrium shapes for OB1. a) Here the light orange curves represent the configurations with Θ extracted from the measurements (colored crosses), and the dark orange are those obtained from modeling after parameter identification. b) Composite image showing the corresponding real object shapes.

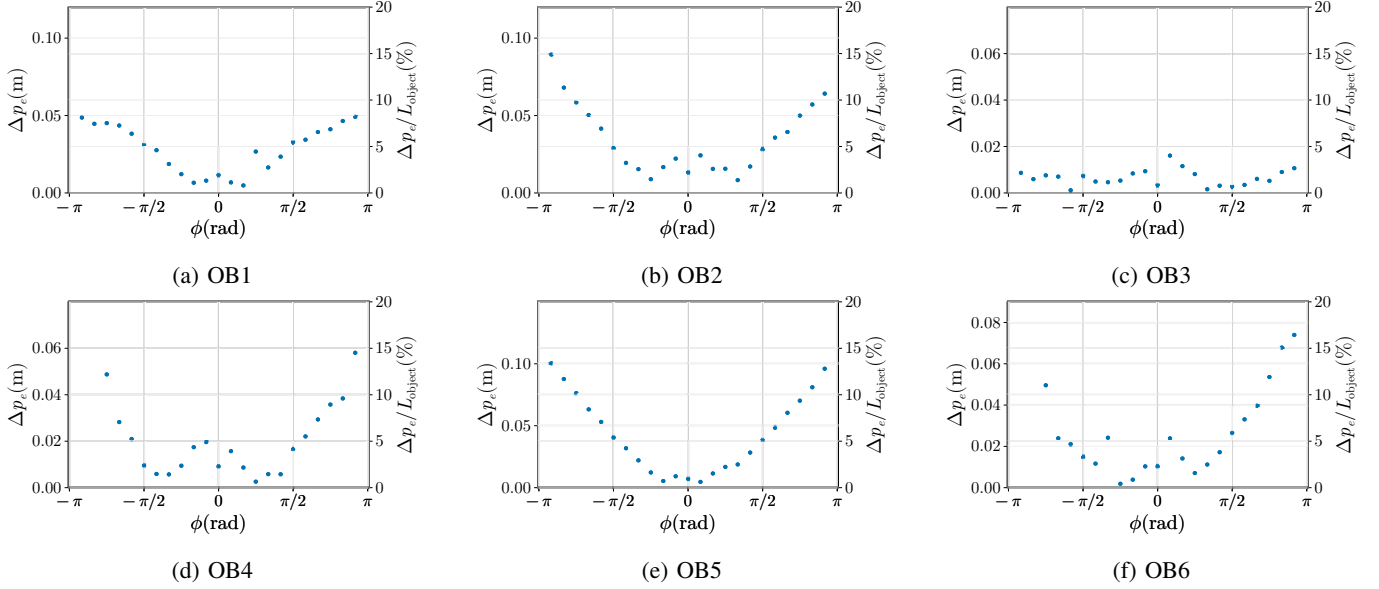


Fig. 8: Error between measured and modeled object endpoint p_e at equilibrium, when the object base is moved to each angle ϕ in the steady state model validation of Section IV-E1.

for the endpoint position in the range $-\frac{3\pi}{4} < \phi < \frac{3\pi}{4}$ for all object types, with an error below 0.05m (8%) in almost all cases. Up to $\phi = \pm\pi$, most types continue to only suffer relatively mild deterioration in accuracy, with some notable exceptions. Most egregiously, OB4 and OB6 display a sudden spike in error for $\phi < -\frac{3\pi}{4}$; on closer inspection, the model with these properties is no longer multi-stable at this point, with the sole equilibrium point biased to the right-hand side of the xy plane due to the offset curvature. This result shows that the in-plane assumption holds for a large range of end effector angles. It also highlights the effect out-of-plane motion of the object has on positioning accuracy. Larger out-of-plane movement is seen at higher angles of ϕ , due to the gravitational forces no longer keeping a sufficient proportion of the object mass below the grasp point, removing this stabilizing effect.

Another limitation of the model is highlighted by OB5, with its worst-case combination of length, stiffness, and endpoint mass resulting in high curvature near the base followed by straightening out along the length. The affine curvature model cannot accurately describe this over a single segment, as will be shown later.

2) *Dynamic Response*: The data for dynamic identification was collected from a single evolution of a pendulum motion for each object with the base fixed. In these experiments, the robot was set to $\phi = 0$, starting from a deformed position far from equilibrium to observe the evolution of the states of the object. Fig. 9a shows a time lapse of the images captured for OB1, along with the detected positions of p_s , p_m and p_e , as well as the Θ configurations from inverse kinematics projected into the camera frame. Note that this shows only the first swing, the full sets of data run until the oscillations cease. This data was used to estimate the value of β , and the resulting fully identified model was then simulated from the same initial conditions. In Fig. 9b this simulated evolution is then projected back onto the same captured images to show

how the simulated object shape compares to the real object in Cartesian space, with only every second frame included for clarity. The time lapse images were not created for each object, but videos are available with the extra materials.

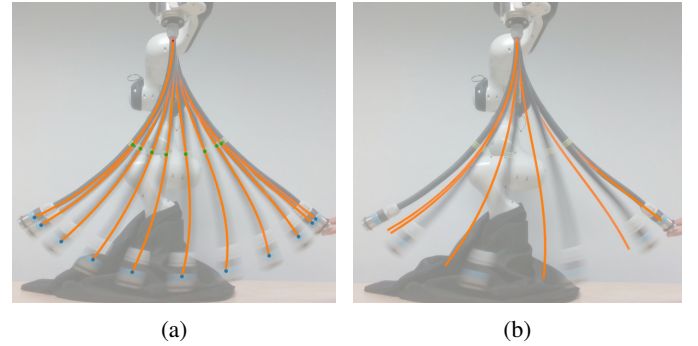


Fig. 9: Partial time lapse comparison of the dynamic evolution of Θ for OB1. The configurations extracted from the images are shown in (a), and the simulated evolution, after using this data for identification, is projected over the captured images in (b), for every second frame only.

Plots comparing the evolution of Θ measured from the experiment and generated by the simulation are shown in Fig. 10. Several of the objects demonstrate quite closely matching responses, though there are some discrepancies for others. This is most obvious when comparing some of the amplitudes, however it is worth noting that as the two components of Θ generally occur with opposite phase, these plots can be a misleading indication of how the object shapes in Cartesian space compare. The discrepancies in the steady-state results are attributed to the hysteresis effect of the DLO, which tends towards the offset configuration, $\bar{\Theta}$. The hysteresis effect causes slight alterations in this configuration producing the errors seen observed in the figure. The sensitivity of our model

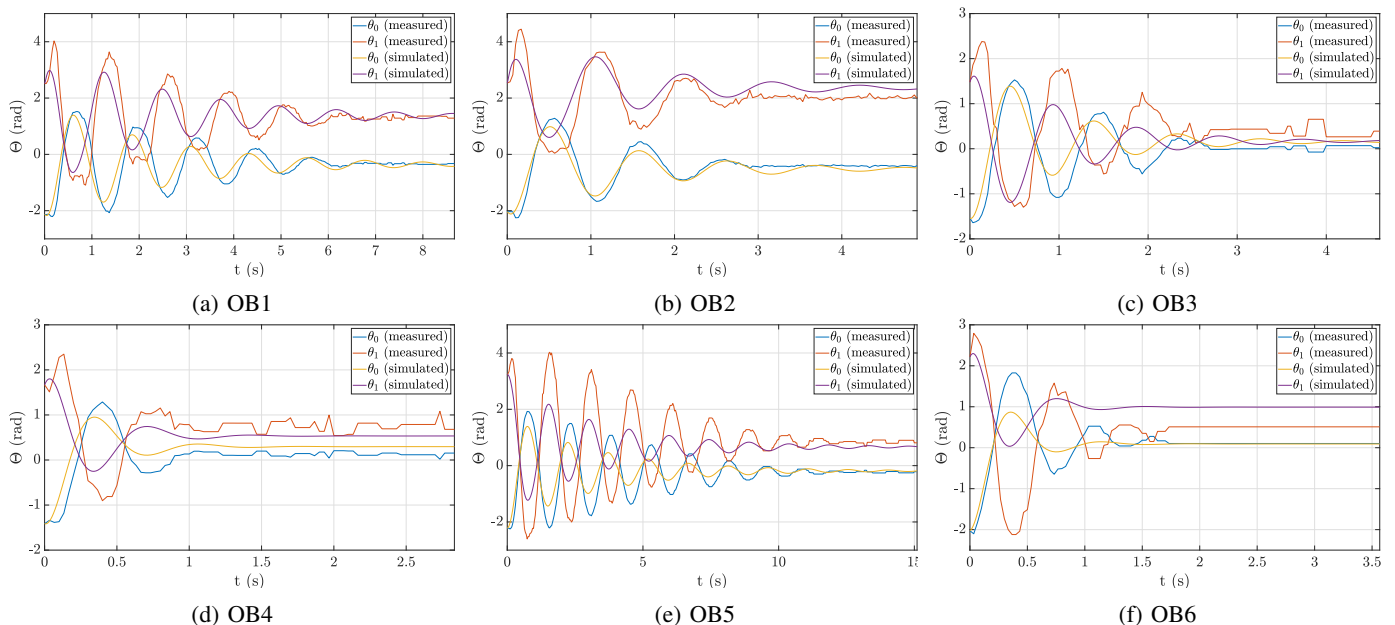


Fig. 10: Comparison between Θ state evolutions undergoing pendulum motion from the dynamic model validation of Section IV-E2. The measured data in the graphs is extracted from the image frames, and the simulated traces are generated from the model using the same initial Θ and with $\dot{\Theta}(t=0) = 0$.

to the hysteresis effect is analyzed in a subsequent section. Conversely, the phase lead in these plots that tends to appear fairly minor for most objects, is more clearly visible in Fig. 9b. The phase lead results from a slight mismatch in the initial state guess used during the dynamic simulation, as observed in Fig. 10. This discrepancy is attributed to minor variations in the parameters of the DLO. These factors make it particularly challenging to establish an accurate initial guess for validating the model. To better evaluate the dynamic evolution of the system, we compare the time evolution of the mid-point and end-effector coordinates of the DLO as observed in the experiment with those generated by our model in simulation, as shown in Fig. 11.

F. Influence of hysteresis in our model

In this section, we have analyzed the effect of hysteresis for a specific object (OB1) to quantify this effect in our model. Our observations indicate that the hysteresis effect of DLO can be effectively captured by adjusting the offset Θ in the elastic force term. In the model, this parameter was identified to minimize the error across various shapes and was kept constant. However, we observed that if this parameter Θ is identified separately for each case, its value can vary in the range $[-2\hat{\theta}_i, 2\hat{\theta}_i]$ considering that $\hat{\theta}_i$ is the nominal value (see Table II).

Taking this into account, we performed a sensitivity analysis to examine how the shapes and errors change within this range for different configurations. The results of this analysis are presented in Fig. 12 where we analyze the sensitivity of our model to the hysteresis effect under different orientations of the robot's end-effector. This effect results in an average error of 5 % and 7.5 % of the DLO's length at the midpoint and

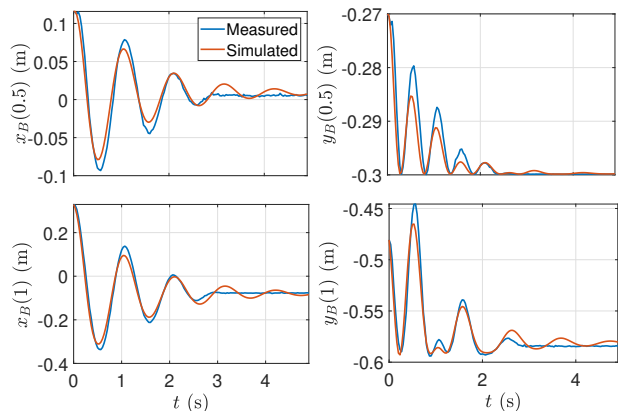


Fig. 11: Comparison of the end-effector coordinates of the DLO to evaluate the dynamic evolution of the system for OB2.

endpoint, respectively. The error can be significantly reduced by loosening the DLO through shaking prior to conducting an experiment.

V. EXPERIMENTAL VALIDATION OF THE CONTROLLER

The control framework was experimentally validated, focusing on control of the object endpoint as a practical goal specification. Due to the underactuated nature of DLO, not all configurations are attainable, as they must satisfy the static equilibrium condition. Therefore, we propose solving the kinematic inversion of our model for a given desired task coordinate that satisfies the static equilibrium condition through an optimization process.

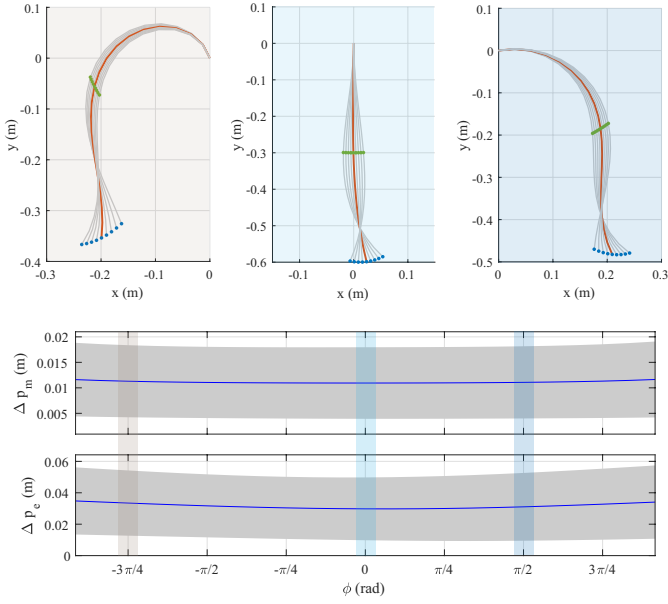


Fig. 12: Influence of hysteresis for different configurations within the observed experimental range. The nominal case is plotted with an orange line in the upper part, while the different shapes using hysteresis are shown in grey.

A. Position

In the first case we look at positioning the object endpoint at a goal p^* only, so that $\zeta = p_e$, and take the Euclidean distance error as the optimization cost. We use a circular constraint on the floating base coordinates to represent the workspace of the manipulator, specifically a circle of radius 0.5m centred at $(0, 0.333)$ in $\{S_B\}$, which approximates the reach of the FR3. Since the modeling accuracy and planar assumption start to deteriorate at higher base orientations, it was also decided to limit the range of angles to $-\frac{3\pi}{4} \leq \phi \leq \frac{3\pi}{4}$. The optimization problem is therefore:

$$\begin{aligned} & \min_{\Theta^* \in \mathbb{R}^{n+1}, \{x^*, y^*, \phi^*\} \in \mathbb{F}} \|p^* - p_e(x^*, y^*, \phi^*, \Theta^*)\|_2 \\ & \text{s.t. } G_{\Theta}(\Theta^*, \phi^*) + kH(\Theta^* - \bar{\Theta}) = 0 \\ & \mathbb{F} = \{x^2 + (y - 0.333)^2 - 0.5^2 \leq 0\} \times \left\{-\frac{3\pi}{4} \leq \phi \leq \frac{3\pi}{4}\right\}. \end{aligned} \quad (24)$$

We used the controller to position the object endpoint by solving (24) at each point of a grid of endpoint goals, with 0.1m spacing. The grid covers an area in $\{S_B\}$ of $-0.7 \leq x \leq 0.7$ m and $0.05 \leq y \leq 0.75$ m, although depending on the object type it may not be necessary to cover the full height in the y -direction once it exceeds the reachable range. The MATLAB `fmincon` solver was used to obtain the solutions, and results were obtained for OB1, OB2, OB3 and OB5, as their properties cover a wide range of high deformation behaviour. Additionally, a 'model-free' reference was evaluated to compare our method with alternative strategy for positioning the DLO's end-effector, without considering its curvature model. This strategy involves constraining $\phi = 0$ and positioning the manipulator at a constant offset to p^* (or as close as possible, given the manipulator's workspace

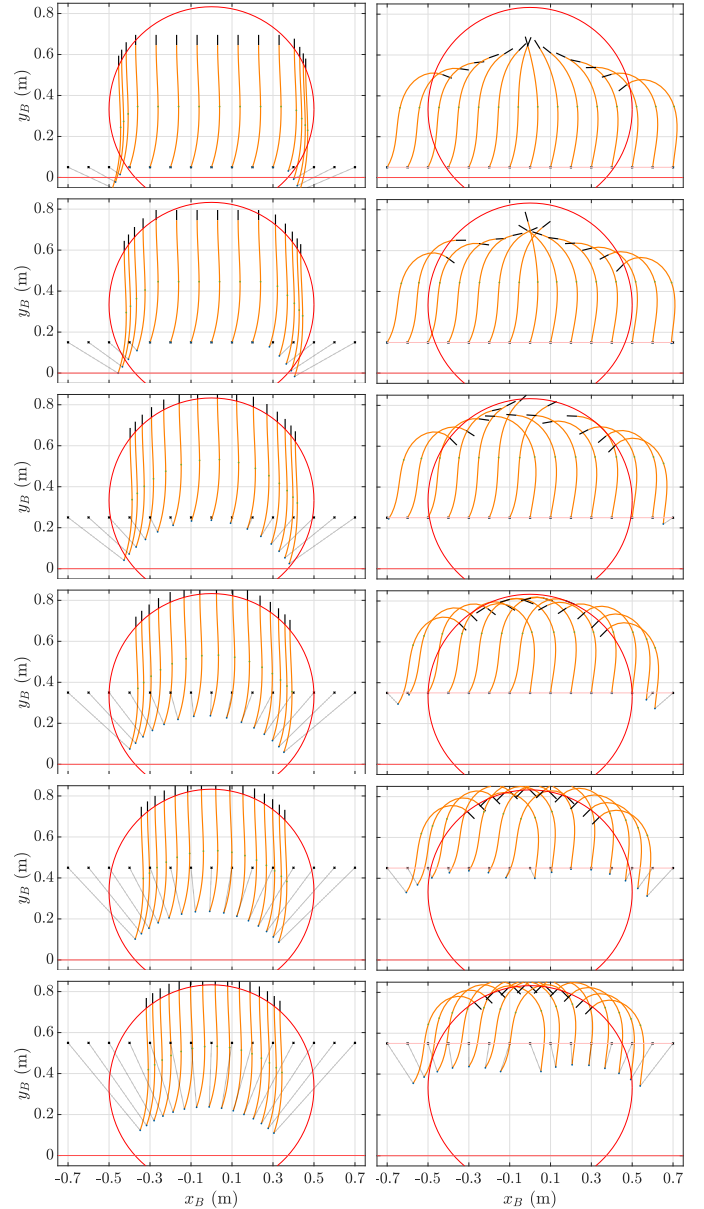


Fig. 13: Solutions generated by the optimization (24) for OB1 in the endpoint positioning experiment described in Section V-A. The model-free reference case is shown on the left, and the model-based case on the right. The endpoint goal positions are marked with small crosses, and lines are drawn to the achievable optimized solution.

constraint), which is derived from the measured steady state p_e .

Fig. 13 shows the manipulator solutions and corresponding equilibrium configurations of the modeled object for each row of the workspace validation in both cases for OB1. Lines are drawn pairing the goals with the achieved modeled endpoints, and the red circle indicates the constraint placed on the manipulator endpoint position.

Based on these solutions, we assess the controller experimentally by measuring p_e after moving the manipulator to each configuration, as demonstrated in the example image

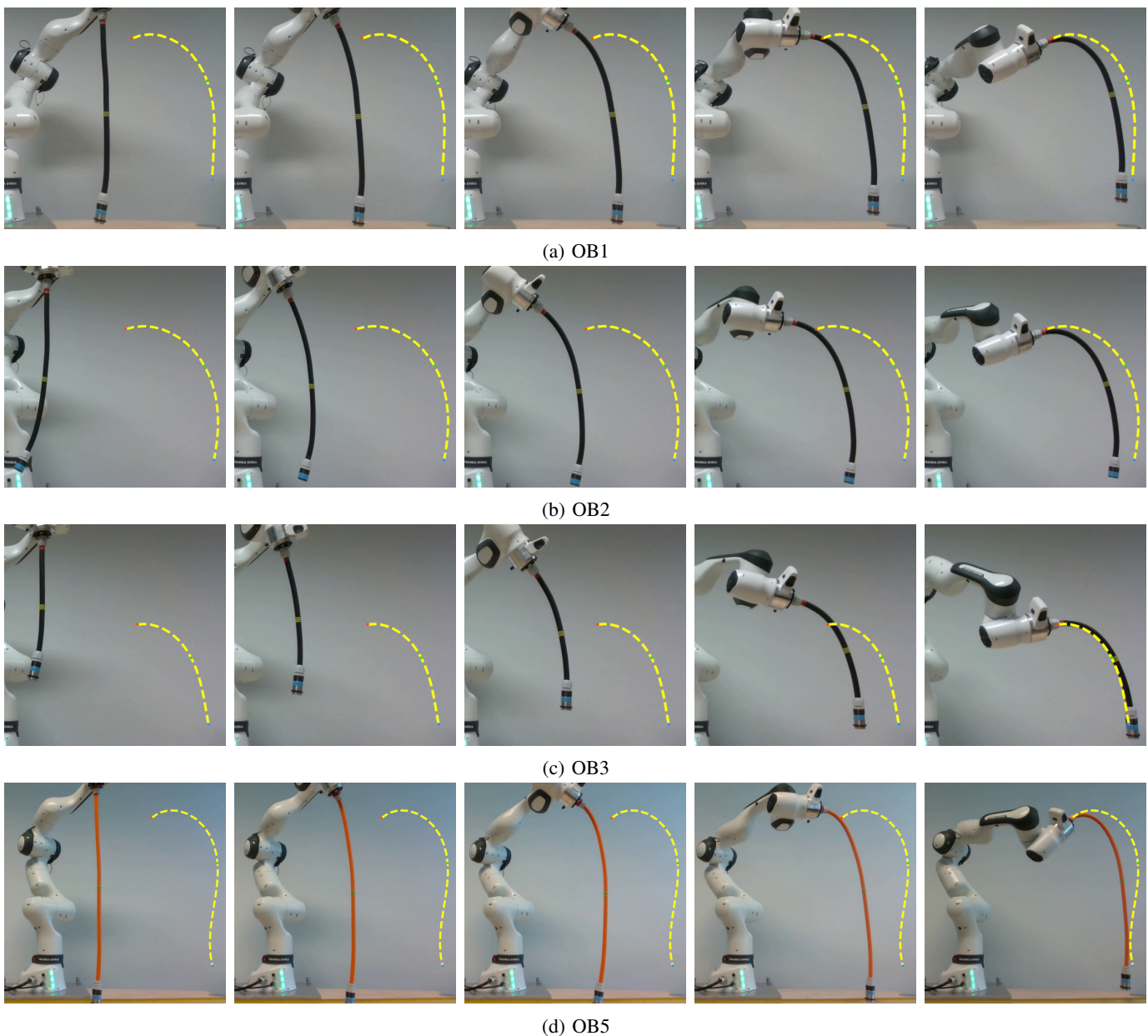


Fig. 14: Example image sequences from the endpoint position control validation experiment in Section V-A, showing the manipulator moving to the desired object configurations corresponding to target endpoint goal locations. The dashed overlays indicate the intended final object goal states generated by the model-constrained optimization (24).

sequences in Fig. 14.

The results of these experiments carried out throughout the whole grid are summarized in Fig. 15, where the grid colors correspond to the error between the goal p^* , located at the center of each cell, and p_e .

For all objects it is clear that the endpoint reachability is significantly expanded compared to the 'model-free' reference case, as expected. The measured positioning accuracy in this increased workspace varies significantly, generally corresponding to decreased accuracy with the use of larger $|\phi|$. The model-based case is clearly an improvement based on these demonstrations. Measuring the mean endpoint error over all measured grid points, there is a reduction in the

measured mean error compared to the 'model-free' reference case of 63.0%, 68.1%, 78.5% and 57.7% for the four objects respectively.

B. Orientation

Here we continue assessing the reachable workspace of the object's endpoint, now focussing only on the orientation, i.e. the accuracy of positioning p_e at a single location in $\{S_B\}$ but with the tip pointed in a specified angle. We will refer to the angle of the tip as $\psi_{e,B'} = \phi + \alpha_e$, note that this is in the $\{S_{B'}\}$ frame so that pointing directly downwards corresponds to 0. For this validation we only investigate OB4 and OB6, as inspection of the static identification results indicated a very

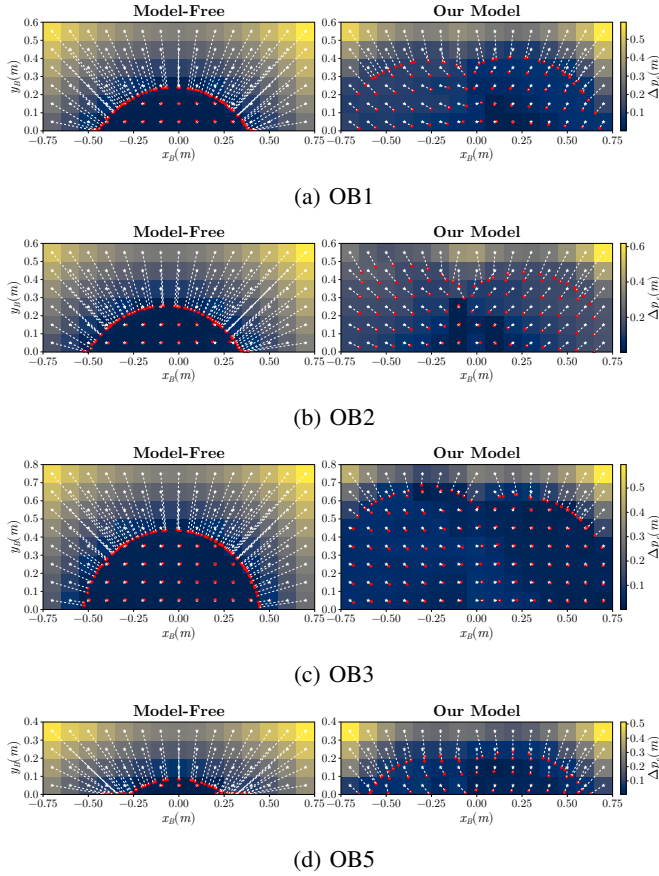


Fig. 15: Visualization of the endpoint positioning accuracy over the workspace for OB1, OB2, OB3 and OB5. The plots (a) - (d), show the results of experiments to compare the model-free strategy and our model-based controller with shape regulation. The centre of each cell was the goal of the controller p^* (white star). The intensity of the cell color indicates the error for that goal p_e . The red dot shows the measured position of the objects's endpoint. A white dashed line is drawn between each goal and the measured point

limited achievable tip angle range for the other objects, due to their length and weight.

The experimental process is similar to that in Section V-A, now with $\zeta = (p_e, \psi_{e,B'})$ requiring the addition of the endpoint orientation error into the optimization cost. We simplify by ensuring the endpoint position goal p^* is always exactly reachable by removing workspace position constraints on the manipulator, and only target endpoint orientation goals $\psi_{B'}^*$ away from $\pm\pi$, so it is sufficient to define d as the 2-norm of the combined position and angle errors. We relax the constraint on the manipulator angle to $-\frac{3\pi}{4} \leq \phi < \pi$, which allows a goal range of $-\frac{\pi}{2} \leq \psi_{B'}^* \leq \frac{\pi}{2}$. Hence the optimization problem here is:

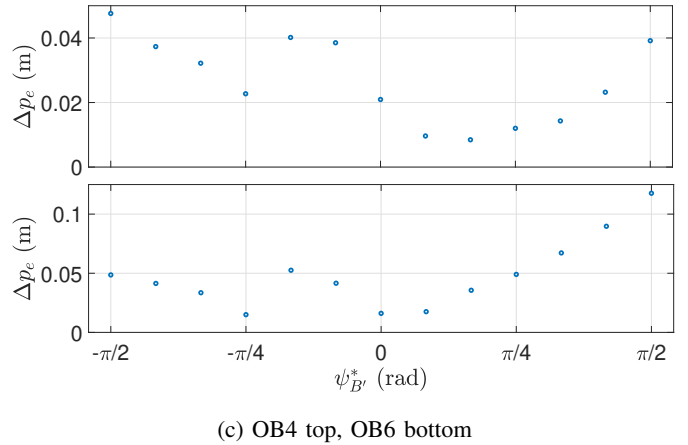
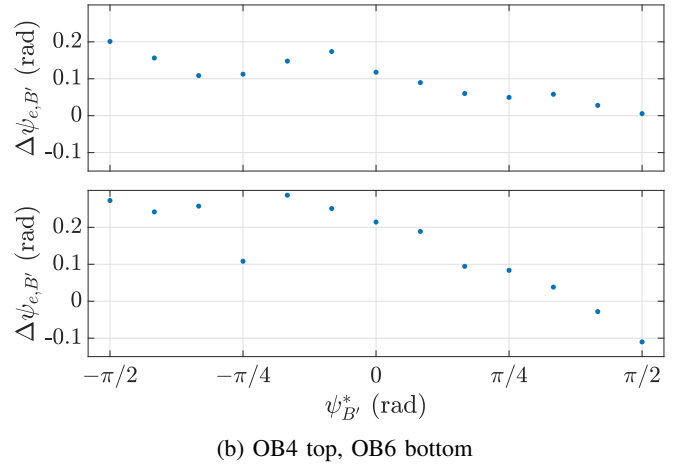
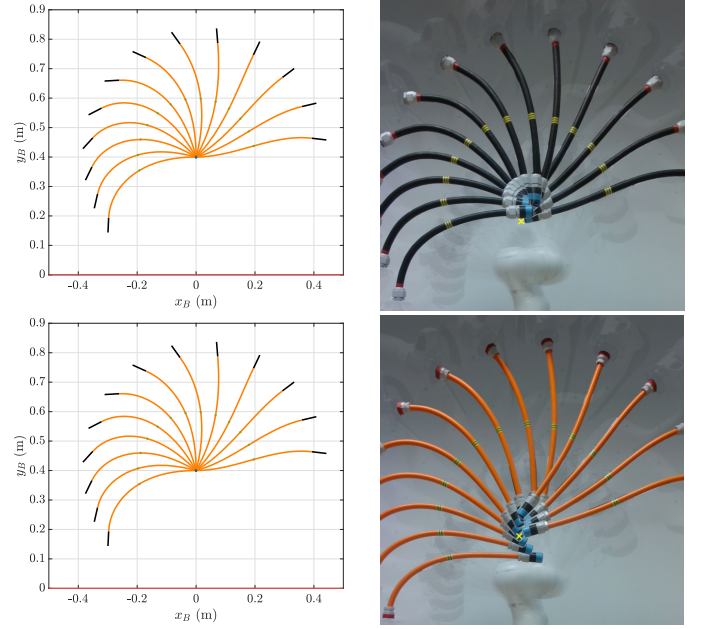


Fig. 16: (a) Solutions generated by the optimization (25) for the endpoint orientation control experiment in Section V-B, and composites of the corresponding real object states. The yellow cross indicates the intended endpoint position. (b) Error between the goal and measured object tip angles. (c) Position errors between the goal and measured object tip position.

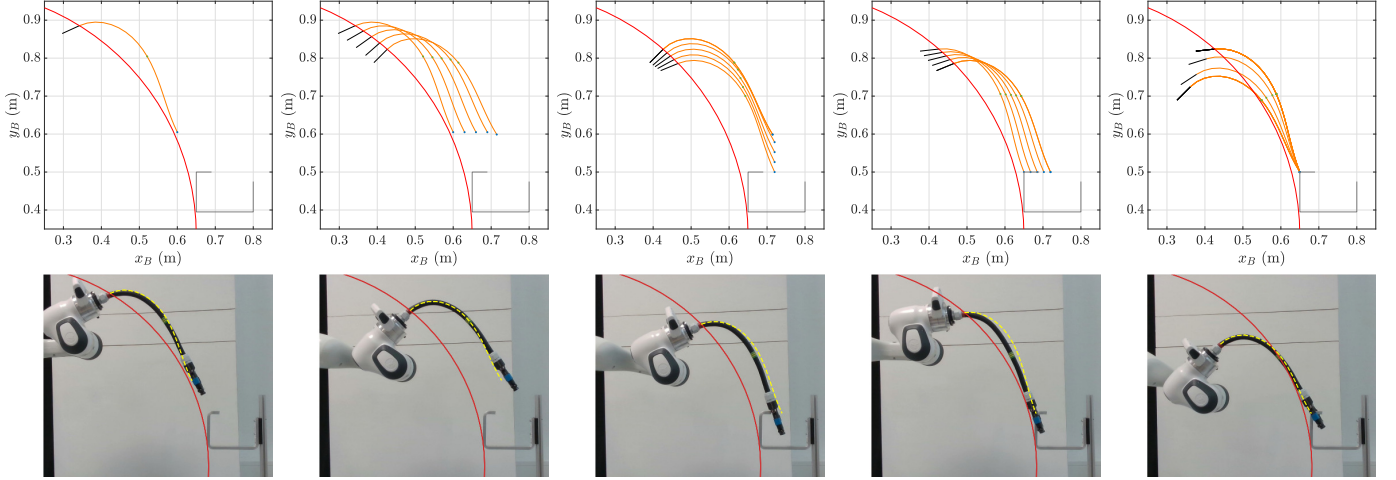


Fig. 17: Results from the object hooking task demonstration. The base position and object configurations generated for a series of endpoint goal locations are shown above, with corresponding images from the experiment below, overlaid with the intended object configuration at that time, and the radial constraint on the manipulator endpoint.

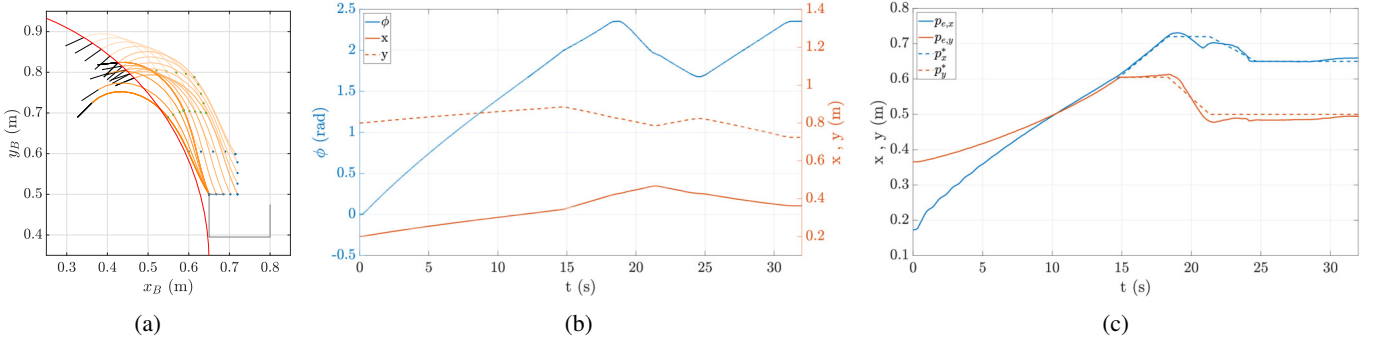


Fig. 18: (a) The complete series of object configurations generated for the hooking task. (b) The measured trajectory of the object base during the experiment. Note that until $t = 15s$ the manipulator is moving to the first generated trajectory point in the series. (c) The measured trajectory of the object endpoint coordinates, as well as the reference endpoint goal trajectory.

$$\begin{aligned}
 & \min_{\Theta^* \in \mathbb{R}^{n+1}, (x^*, y^*, \phi^*) \in \mathbb{F}} \left\| \begin{matrix} p^* - p_e(x^*, y^*, \phi^*, \Theta^*) \\ \psi_{B'}^* - \psi_{e,B'}(\phi^*, \Theta^*) \end{matrix} \right\|_2 \\
 & \text{s.t. } G_{\Theta}(\Theta^*, \phi^*) + kH(\Theta^* - \bar{\Theta}) = 0 \\
 & \mathbb{F} = \left\{ \frac{-3\pi}{4} \leq \phi \leq \pi \right\}.
 \end{aligned} \quad (25)$$

Solving the problem for $\psi_{B'}^* \in [-\frac{\pi}{2}, \frac{\pi}{2}]$ at $\frac{\pi}{12}$ rad increments and $p^* = (0, 0.4)$ produced the configurations shown in the plots on the left of Fig. 16a, with composites of the real object state at each of these configurations displayed on the right.

To quantitatively assess the accuracy, the angle of the tip was determined by measuring the points at the start and end of the endpoint weight to obtain a direction vector in the xy plane. The error between this and the goal angle is plotted in Fig. 16b. The position errors are also plotted in Fig. 16c. This investigation also reveals considerable ability to reach specified orientations in the range $-\frac{\pi}{2} \leq \psi_{B'}^* \leq \frac{\pi}{2}$, with a recorded maximum absolute angle error of around 0.29 rad or 17°. Particularly in the range of $0 \leq \psi_{B'}^* \leq \frac{\pi}{2}$ the error is maintained below 0.12 rad (7°) and 0.21 rad (12°) for OB4

and OB6 respectively. The position errors are also small, with most cases being below 10% of the object's length.

C. Task Demonstration

As a further demonstration using the controller in a task oriented manner, we provide an example where the robot needs to hang the end of the object over a hook which lies outside the reachable workspace of both the robot end effector, and the object endpoint when in the reference vertical configuration. Five main goal locations for the endpoint were defined to accomplish this task, with additional intermediate waypoints interpolated in between them. The first four locations involve varying the position of the object endpoint while keeping its orientation constant. The final location maintains a fixed position while rotating the end effector by $\pi/4$ radians. We then use the optimisation procedure for this series of goals to generate a trajectory for the object base pose, and execute this with the robot manipulator.

The upper row of Fig. 17 shows the generated configurations at the main goals, as well as the intermediate points, and images captured at these locations during the experiment are

shown below, with the modeled object state and manipulator endpoint constraint overlaid (a video of the complete experiment is shown in the multimedia attachment). The complete set of configurations are shown together in Fig. 18a, and the measured trajectory of the object base and the x - and y -coordinates of the object endpoint along with its intended goal path are plotted in Fig. 18b and Fig. 18c, respectively.

VI. CONCLUSION

We presented a strain-based modeling approach for manipulating deformable linear objects, using a polynomial curvature parametrization developed within the context of soft robotics to enable compact, model-based control. The manipulation task was framed as a control problem, and controllers with provable guarantees were introduced. We focused in this work on planar bending (i.e., curvature only), but additional strains such as torsion can be added to demonstrate 3D manipulation. Results in simulations show that choosing a higher-order polynomial to describe the system's curvature improves accuracy but comes at the cost of increased computational time when solving the optimization problems. Thus, for this paper, we opted for the linear curvature model as a compromise between accuracy and simplicity when it came to experimental validation. Experiments showed that even minimal models can achieve steady-state accuracy across various object properties, outperforming model-free baselines by 57.7–78.5% in positioning, with maximum orientation errors of 12° and 17°. We also demonstrated task-level applications and assessed dynamic model accuracy. Future work will focus on validating experimentally higher-order strain models, non-collocated feedback, dynamic motions involving trajectory tracking, and fast actions such as throwing or whipping.

REFERENCES

- [1] V. E. Arriola-Rios and et al., "Modeling of deformable objects for robotic manipulation: A tutorial and review," *Frontiers Robot. AI*, vol. 7, p. 82, 2020.
- [2] H. Yin and et al., "Modeling, learning, perception, and control methods for deformable object manipulation," *Science Robotics*, vol. 6, no. 54, p. eabd8803, 2021.
- [3] J. Zhu and et al., "Challenges and outlook in robotic manipulation of deformable objects," *IEEE Robot. & Automat. Magazine*, vol. 29, no. 3, pp. 67–77, 2022.
- [4] P. Fiorini and et al., "Concepts and trends in autonomy for robot-assisted surgery," *Proceedings of the IEEE*, vol. 110, no. 7, pp. 993–1011, 2022.
- [5] M. T. Mason and et al., "Robot hands and the mechanics of manipulation," 1985.
- [6] A. Bicchi, "On the problem of decomposing grasp and manipulation forces in multiple whole-limb manipulation," *Robot. and Auton. Syst.*, vol. 13, no. 2, pp. 127–147, 1994.
- [7] N. C. Daffe and et al., "Extrinsic dexterity: In-hand manipulation with external forces," in *2014 IEEE Int. Conf. Robot. Automat.* IEEE, 2014, pp. 1578–1585.
- [8] T. Pang and et al., "Global planning for contact-rich manipulation via local smoothing of quasi-dynamic contact models," *IEEE Trans. Robot.*, 2023.
- [9] D. Navarro-Alarcon and et al., "Model-free visually servoed deformation control of elastic objects by robot manipulators," *IEEE Trans. Robot.*, vol. 29, no. 6, pp. 1457–1468, 2013.
- [10] J. Zhu and et al., "Dual-arm robotic manipulation of flexible cables," in *2018 IEEE/RSJ Int. Conf. Intell. Robots Syst.* IEEE, 2018, pp. 479–484.
- [11] R. Lagneau and et al., "Active deformation through visual servoing of soft objects," in *2020 IEEE Int. Conf. Robot. Automat.* IEEE, 2020, pp. 8978–8984.
- [12] J. Zhu and et al., "Vision-based manipulation of deformable and rigid objects using subspace projections of 2d contours," *Robot. Auton. Syst.*, vol. 142, p. 103798, 2021.
- [13] M. Shetab-Bushehri and et al., "As-rigid-as-possible shape servoing," *IEEE Robot. Automat. Lett.*, vol. 7, no. 2, pp. 3898–3905, 2022.
- [14] H. Wakamatsu and S. Hirai, "Static modeling of linear object deformation based on differential geometry," *The Int. J. Robot. Research*, vol. 23, no. 3, pp. 293–311, 2004.
- [15] M. Yu and et al., "Shape control of deformable linear objects with offline and online learning of local linear deformation models," in *2022 Int. Conf. Robot. Automat.* IEEE, 2022, pp. 1337–1343.
- [16] M. C. Nah and et al., "Dynamic primitives facilitate manipulating a whip," in *2020 8th IEEE RAS/EMBS Int. Conf. for Biomedical Robot. and Biomechatronics.* IEEE, 2020, pp. 685–691.
- [17] H. Zhang and et al., "Robots of the lost arc: Self-supervised learning to dynamically manipulate fixed-endpoint cables," in *2021 IEEE Int. Conf. Robot. Automat.* IEEE, 2021, pp. 4560–4567.
- [18] X. Lin and et al., "Softgym: Benchmarking deep reinforcement learning for deformable object manipulation," in *Conference on Robot Learning.* PMLR, 2021, pp. 432–448.
- [19] V. Lim and et al., "Real2sim2real: Self-supervised learning of physical single-step dynamic actions for planar robot casting," in *2022 International Conference on Robotics and Automation (ICRA)*, 2022, pp. 8282–8289.
- [20] C. Chi and et al., "Iterative residual policy: for goal-conditioned dynamic manipulation of deformable objects," *arXiv preprint arXiv:2203.00663*, 2022.
- [21] F. Liu and et al., "Robotic manipulation of deformable rope-like objects using differentiable compliant position-based dynamics," *IEEE Robot. Automat. Lett.*, 2023.
- [22] A. Caporali and et al., "A weakly supervised semi-automatic image labeling approach for deformable linear objects," *IEEE Robot. Automat. Lett.*, vol. 8, no. 2, pp. 1013–1020, 2023.
- [23] S. Kuroki and et al., "Generalizable one-shot rope manipulation with parameter-aware policy," *arXiv preprint arXiv:2306.09872*, 2023.
- [24] A. Caporali and et al., "Deformable linear objects manipulation with online model parameters estimation," *IEEE Robot. Automat. Lett.*, 2024.
- [25] N. Lv and et al., "Dynamic modeling and control of deformable linear objects for single-arm and dual-arm robot manipulations," *IEEE Trans. Robot.*, vol. 38, no. 4, pp. 2341–2353, 2022.
- [26] A. Macchelli and et al., "Port-based modeling of a flexible link," *IEEE Trans. Robot.*, vol. 23, no. 4, pp. 650–660, 2007.
- [27] M. Tognon and et al., "Aerial co-manipulation with cables: The role of internal force for equilibria, stability, and passivity," *IEEE Robot. Automat. Lett.*, vol. 3, no. 3, pp. 2577–2583, 2018.
- [28] K. D. Do, "Stabilization of exact nonlinear timoshenko beams in space by boundary feedback," *J. Sound Vibration*, vol. 422, pp. 278–299, 2018.
- [29] A. Mattioni and et al., "Modelling and control of an ipmc actuated flexible structure: A lumped port hamiltonian approach," *Control Engineering Practice*, vol. 101, p. 104498, 2020.
- [30] C. Gabellieri and A. Franchi, "Differential flatness and manipulation of elasto-flexible cables carried by aerial robots in a possibly viscous environment," in *2023 Int. Conf. Unmanned Aircraft Syst.* IEEE, 2023, pp. 963–968.
- [31] C. Della Santina and et al., "Model-based control of soft robots: A survey of the state of the art and open challenges," *IEEE Control Syst. Magazine*, vol. 43, no. 3, pp. 30–65, 2023.
- [32] D. Rus and M. T. Tolley, "Design, fabrication and control of soft robots," *Nature*, vol. 521, no. 7553, pp. 467–475, 2015.
- [33] C. Della Santina and et al., "Soft robots," *Encyclopedia of Robotics*, 2021.
- [34] C. Armanini and et al., "Soft robots modeling: A structured overview," *IEEE Trans. Robot.*, vol. 39, no. 3, pp. 1728–1748, 2023.
- [35] B. J. Caasenbrood and et al., "Sorotoki: A matlab toolkit for design, modeling, and control of soft robots," *IEEE Access*, 2024.
- [36] D. Navarro-Alarcon and Y.-H. Liu, "Fourier-based shape servoing: a new feedback method to actively deform soft objects into desired 2-d image contours," *IEEE Trans. Robot.*, vol. 34, no. 1, pp. 272–279, 2017.
- [37] J. Qi and et al., "Adaptive shape servoing of elastic rods using parameterized regression features and auto-tuning motion controls," *IEEE Robot. Automat. Lett.*, vol. 9, no. 2, pp. 1428–1435, 2023.
- [38] G. Palli, "Model-based manipulation of deformable linear objects by multivariate dynamic splines," in *2020 IEEE Conf. Industrial Cyber-physical Syst.*, vol. 1. IEEE, 2020, pp. 520–525.
- [39] S. H. Sadati and et al., "Control space reduction and real-time accurate modeling of continuum manipulators using ritz and ritz-galerkin methods," *IEEE Robot. Automat. Lett.*, vol. 3, no. 1, pp. 328–335, 2017.

IEEE Transactions on Robotics (T-RO) paper, presented at ICRA 2026, Vienna, Austria. Cite as T-RO paper.

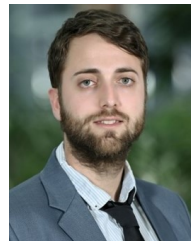
- [40] Z. Wu and et al., "Towards a physics-based model for steerable eversion growing robots," *IEEE Robot. Automat. Lett.*, vol. 8, no. 2, pp. 1005–1012, 2023.
- [41] S. Grazioso and et al., "A geometrically exact model for soft continuum robots: The finite element deformation space formulation," *Soft Robot.*, vol. 6, no. 6, pp. 790–811, 2019.
- [42] F. Renda and et al., "A geometric variable-strain approach for static modeling of soft manipulators with tendon and fluidic actuation," *IEEE Robot Automat. Lett.*, vol. 5, no. 3, pp. 4006–4013, 2020.
- [43] C. Della Santina, "The soft inverted pendulum with affine curvature," in *2020 59th IEEE Conf. Decision Control*. IEEE, 2020, pp. 4135–4142.
- [44] F. Stella and et al., "An experimental validation of the polynomial curvature model: Identification and optimal control of a soft underwater tentacle," *IEEE Robot. Automat. Lett.*, vol. 7, no. 4, pp. 11410–11417, 2022.
- [45] T. George Thuruthel and et al., "Control strategies for soft robotic manipulators: A survey," *Soft robotics*, vol. 5, no. 2, pp. 149–163, 2018.
- [46] H.-S. Chang and et al., "Energy shaping control of a cybertopus soft arm," in *2020 59th IEEE Conference on Decision and Control (CDC)*. IEEE, 2020, pp. 3913–3920.
- [47] E. Franco and et al., "Adaptive energy shaping control of a class of non-linear soft continuum manipulators," *IEEE/ASME Trans. Mechatronics*, vol. 27, no. 1, pp. 280–291, 2021.
- [48] Z. J. Patterson and et al., "Robust control of a multi-axis shape memory alloy-driven soft manipulator," *IEEE Robot. Automat. Lett.*, vol. 7, no. 2, pp. 2210–2217, 2022.
- [49] P. Borja and et al., "Energy-based shape regulation of soft robots with unactuated dynamics dominated by elasticity," in *2022 IEEE 5th Int. Conf. Soft Robot*. IEEE, 2022, pp. 396–402.
- [50] F. Renda and et al., "Geometrically-exact inverse kinematic control of soft manipulators with general threadlike actuators' routing," *IEEE Robot Automat. Lett.*, vol. 7, no. 3, pp. 7311–7318, 2022.
- [51] B. Caasenbrood and et al., "Energy-shaping controllers for soft robot manipulators through port-hamiltonian cosserat models," *SN Computer Science*, vol. 3, no. 6, p. 494, 2022.
- [52] F. Stroppa and et al., "Shared-control teleoperation paradigms on a soft-growing robot manipulator," *Journal of Intelligent & Robotic Systems*, vol. 109, no. 2, p. 30, 2023.
- [53] Z. Wang and et al., "Dynamic modeling and control of a soft robotic arm using a piecewise universal joint model," in *2023 IEEE Int. Conf. Robot. Biomimetics*. IEEE, 2023, pp. 1–6.
- [54] F. Renda and et al., "Dynamics and control of soft robots with implicit strain parametrization," *IEEE Robot. Automat. Lett.*, 2024.
- [55] N. Lv and et al., "Dynamic modeling and control of deformable linear objects for single-arm and dual-arm robot manipulations," *IEEE Trans. Robot.*, vol. 38, no. 4, pp. 2341–2353, 2022.
- [56] Y. Tang and et al., "Learning-based mpc with safety filter for constrained deformable linear object manipulation," *IEEE Robot. Automat. Lett.*, vol. 9, no. 3, pp. 2877–2884, 2024.
- [57] A. Caporali and G. Palli, "Robotic manipulation of deformable linear objects via multiview model-based visual tracking," *IEEE/ASME Trans. Mechatronics*, 2025.
- [58] B. Aksoy and J. Wen, "Planning and control for deformable linear object manipulation," *arXiv preprint arXiv:2503.04007*, 2025.
- [59] L. Besselaar and C. Della Santina, "One-shot learning closed-loop manipulation of soft slender objects based on a planar polynomial curvature model," in *2022 IEEE 5th Int. Conf. Soft Robot*. IEEE, 2022, pp. 518–524.
- [60] C. Della Santina and D. Rus, "Control oriented modeling of soft robots: the polynomial curvature case," *IEEE Robot. Automat. Lett.*, vol. 5, no. 2, pp. 290–298, 2019.
- [61] F. Stella and et al., "Piecewise affine curvature model: a reduced-order model for soft robot-environment interaction beyond pcc," in *2023 IEEE Int. Conf. Soft Robot*. IEEE, 2023, pp. 1–7.
- [62] T. Baaij and et al., "Learning 3d shape proprioception for continuum soft robots with multiple magnetic sensors," *Soft Matter*, vol. 19, no. 1, pp. 44–56, 2023.
- [63] M. P. Do Carmo, *Differential geometry of curves and surfaces: revised and updated second edition*. Courier Dover Publications, 2016.
- [64] H. Altenbach and et al., "Cosserat-type rods," *Generalized Continua from the Theory to Engineering Applications*, pp. 179–248, 2013.
- [65] P. Pustina and et al., "Feedback regulation of elastically decoupled underactuated soft robots," *IEEE Robot. Automat. Lett.*, vol. 7, no. 2, pp. 4512–4519, 2022.
- [66] D. Feliu-Talegon and et al., "Dynamic shape estimation of tendon-driven soft manipulators via actuation readings," *IEEE Robot. Automat. Lett.*, 2024.
- [67] C. Della Santina, "The soft inverted pendulum with affine curvature," in *2020 59th IEEE Conf. Decision Control*. IEEE, 2020, pp. 4135–4142.
- [68] M. Trumić and et al., "On the stability of the soft pendulum with affine curvature: open-loop, collocated closed-loop, and switching control," *IEEE Control Syst. Lett.*, vol. 7, pp. 385–390, 2022.



Sebastien Tiburzio received a BEng(Hons) in Mechatronics from the University of Adelaide, Australia, in 2014 and an MSc in Robotics from Delft University of Technology, The Netherlands, in 2023. His research interests are in modelling and control of dynamic systems, particularly for robotic manipulation. He is currently working in the biotechnology industry in automation of biosensor manufacturing.



Tomás Coleman is PhD candidate at the Department of Cognitive Robotics at Delft University of Technology. He received his Bachelor's Degree in Mechanical Engineering from University College Dublin, Ireland, in 2013 and his MSc degree in Mathematical Modelling and Machine Learning from University College Cork, Ireland, in 2020. His research focuses on the robotic manipulation of highly deformable objects.



Daniel Feliu-Talegon is a Post-Doctoral Fellow at the Department of Cognitive Robotics at Delft University of Technology. He received the MSc degree in 2014 and the Ph.D. degree in 2019 from the University of Castilla La Mancha, Spain. His research interests include the fractional dynamics and control systems, dynamic control of flexible robots, control of lightweight manipulators in aerial robotics, and modelling and dynamic control of soft robot manipulators and deformable objects.



Cosimo Della Santina (Senior Member, IEEE) received his Ph.D. degree (cum laude) in robotics from the University of Pisa, Pisa, Italy, in 2019. He is currently an Associate Professor with TU Delft, Delft, The Netherlands, and a Research Scientist with German Aerospace Institute (DLR), Munich, Germany. He was a visiting Ph.D. student and a Postdoc with Computer Science and Artificial Intelligence Laboratory, Massachusetts Institute of Technology, from 2017 to 2019. He was a Senior Postdoc and a Guest Lecturer with the Department of

Informatics, Technical University of Munich, in 2020 and 2021, respectively. His research interest is in providing motor intelligence to physical systems, focusing on elastic and soft robots. Cosimo is a recipient of several awards, including the euRobotics Georges Giralt Ph.D. Award in 2020 and the IEEE RAS Early Academic Career Award in 2023. He is involved as PI in a number of European and Dutch Projects, he is the co-Director of Delft AI Lab SELF, and he is a recipient of a NWO VENI.